INTERNATIONAL JOURNAL FOR NUMERICAL METHODS IN FLUIDS
Int. J. Numer. Meth. Fluids 2003; **42**:929–952 (DOI: 10.1002/fld.557)

A fully hydrodynamic model for three-dimensional, free-surface flows

XinJian Chen*,†

Surface Water Improvement & Management Program, Southwest Florida Water Management District, 7601 Highway 301 North, Tampa, FL 33637, U.S.A.

SUMMARY

The hydrostatic pressure assumption has been widely used in studying water movements in rivers, lakes, estuaries, and oceans. While this assumption is valid in many cases and has been successfully used in numerous studies, there are many cases where this assumption is questionable. This paper presents a three-dimensional, hydrodynamic model for free-surface flows without using the hydrostatic pressure assumption. The model includes two predictor–corrector steps. In the first predictor–corrector step, the model uses hydrostatic pressure at the previous time step as an initial estimate of the total pressure field at the new time step. Based on the estimated pressure field, an intermediate velocity field is calculated, which is then corrected by adding the non-hydrostatic component of the pressure to the estimated pressure field. A Poisson equation for non-hydrostatic pressure is solved before the second intermediate velocity field is calculated. The final velocity field is found after the free surface at the new time step is computed by solving a free-surface correction equation.

The numerical method was validated with several analytical solutions and laboratory experiments. Model results agree reasonably well with analytical solutions and laboratory results. Model simulations suggest that the numerical method presented is suitable for fully hydrodynamic simulations of three-dimensional, free-surface flows. Copyright © 2003 John Wiley & Sons, Ltd.

KEY WORDS: hydrostatic; non-hydrostatic; free-surface flows; 3-D hydrodynamic model; finite difference method; predictor–corrector procedure; free-surface correction (FSC) method

1. INTRODUCTION

The hydrostatic pressure assumption has been widely used in studying flows in rivers, lakes, estuaries, and oceans. This assumption is valid in most cases and has be successfully used in many popular three-dimensional, hydrodynamic models such as the Princeton Ocean Model [1], the Curvilinear Hydrodynamic 3-D model [2], the Environmental Fluid Dynamic Code [3], etc. The basic idea of this assumption comes from the fact that due to a much smaller vertical

*Correspondence to: XinJian Chen, Surface Water Improvement & Management Program, Southwest Florida Water Management District, 7601 Highway 301 North, Tampa, FL 33637, U.S.A.
†E-mail: xinjian.chen@swfwmd.state.fl.us

Received 18 December 2002
Revised 11 March 2003

length scale in comparison with the horizontal length scales, the acceleration and eddy viscosity terms in the momentum equation for the vertical velocity component are much smaller than the gravitational acceleration and can thus be neglected. Nevertheless, there are many cases where this assumption may be questionable. One example is the flow induced by a strong horizontal density gradient. Other examples include short waves, flows controlled by structures, and near-field problems (e.g. the brine disposal from a desalination plant, the uptake point of a water withdrawal system, etc.). In all these cases, effects of non-hydrostatic pressure on flow may be comparable to hydrostatic pressure, and thus cannot be neglected in model simulations.

There exist only a limited number of 3-D models that are capable of including non-hydrostatic pressure in the simulation. Casulli's semi-implicit model is one of them [4, 5]. Mahadevan *et al.* [6] developed a non-hydrostatic mesoscale ocean model that used the similar solution procedure as that of Casulli's model, although the former used a control volume method, while the latter used a finite difference method. Jankowski [7] modified an existing finite element code by adding non-hydrodynamic component to it. Recently, Koçyigit *et al.* [8] developed a non-hydrostatic model that follows the same procedure as that of Cassuli and Mahadevan *et al.*, but uses the so-called sigma-co-ordinate in the vertical direction to discretize the water depth. All these non-hydrostatic models employ an operator-splitting (fractional step) technique that splits the differential operator in the momentum equation into several parts according to their physical processes. The original momentum equation is thus split into a few simpler equations, each containing only portion(s) of all physical processes. The original momentum equation is then treated as the summation of the simpler equations. One of the simpler equations considers only the non-hydrostatic effects.

This study developed a fully hydrodynamic model for three-dimensional, free-surface flows with a slightly different approach. The Reynolds averaged Navier–Stokes (RANS) equations are solved using a double predictor–corrector procedure. In the first predictor–corrector step, an intermediate velocity field is predicted using the hydrostatic pressure field at the previous time step. It is then corrected after a Poisson equation for non-hydrostatic pressure is solved. The equation for non-hydrostatic pressure is obtained by forcing the velocity field divergence-free. The corrected velocity field with the consideration of non-hydrostatic pressure is further corrected in the second predictor–corrector step after a free-surface correction (FSC) method is used to find the location of the final free-surface elevation. In this simulation procedure, the hydrostatic simulation is a special case and can be carried out without performing the first predictor–corrector step.

The numerical scheme was tested with two analytical solutions, including a deepwater standing wave and a second mode seiching in a rectangular basin with finite amplitude. It was also tested with laboratory experiments that were used to validate some previous non-hydrostatic models [5, 7], including a so-called lock-exchange case where the baroclinic force is pivotal and a steep wave propagating over a bar. The model was run both with and without the non-hydrostatic effects for all four test cases. Because non-hydrostatic effects in these cases are important, model runs with the consideration of non-hydrostatic pressure generated much better model results than those generated by model runs without the non-hydrostatic effects.

In the following, governing equations for free-surface flows are first presented before the numerical scheme is described. Tests of the numerical scheme using two analytical solutions and some laboratory experiments are then given. Model results and their comparisons with analytical solutions and laboratory experiments are discussed, before conclusions are drawn.

2. GOVERNING EQUATIONS

The model solves the following RANS equations, including the continuity and momentum equations

$$\frac{\partial u}{\partial x}+\frac{\partial v}{\partial y}+\frac{\partial w}{\partial z}=0 \tag{1}$$

$$\frac{\partial u}{\partial t}+\frac{\partial uu}{\partial x}+\frac{\partial vu}{\partial y}+\frac{\partial wu}{\partial z}=fv-\frac{1}{\rho}\frac{\partial p}{\partial x}+\frac{\partial}{\partial x}\left(A_{\mathrm{h}}\frac{\partial u}{\partial x}\right)+\frac{\partial}{\partial y}\left(A_{\mathrm{h}}\frac{\partial u}{\partial y}\right)+\frac{\partial}{\partial z}\left(A_{\mathrm{v}}\frac{\partial u}{\partial z}\right) \tag{2}$$

$$\frac{\partial v}{\partial t}+\frac{\partial uv}{\partial x}+\frac{\partial vv}{\partial y}+\frac{\partial wv}{\partial z}=-fu-\frac{1}{\rho}\frac{\partial p}{\partial y}+\frac{\partial}{\partial x}\left(A_{\mathrm{h}}\frac{\partial v}{\partial x}\right)+\frac{\partial}{\partial y}\left(A_{\mathrm{h}}\frac{\partial v}{\partial y}\right)+\frac{\partial}{\partial z}\left(A_{\mathrm{v}}\frac{\partial v}{\partial z}\right) \tag{3}$$

$$\frac{\partial w}{\partial t}+\frac{\partial uw}{\partial x}+\frac{\partial vw}{\partial y}+\frac{\partial ww}{\partial z}=-g-\frac{1}{\rho}\frac{\partial p}{\partial z}+\frac{\partial}{\partial x}\left(A_{\mathrm{h}}\frac{\partial w}{\partial x}\right)+\frac{\partial}{\partial y}\left(A_{\mathrm{h}}\frac{\partial w}{\partial y}\right)+\frac{\partial}{\partial z}\left(A_{\mathrm{v}}\frac{\partial w}{\partial z}\right) \tag{4}$$

where t is time; x, y, and z are Cartesian co-ordinates (x is from west to east, y from south to north, and z vertical pointing upward); u, v, and w are velocities in the x-, y-, and, z-directions, respectively; g, η, ρ, and p denote the gravitational acceleration, the free-surface elevation, density, and pressure, respectively; A_{h} and A_{v} represent horizontal and vertical eddy viscosities, respectively; and f ($=2\Omega\sin\phi$, where Ω is the angular rotation velocity of the earth and ϕ is the latitude) is the Coriolis parameter. For very large open water bodies at the low latitude (e.g. the Gulf of Mexico), Mahadevan *et al.* [6] found that the Coriolis acceleration component in the vertical direction should be included in Equation (4). The inclusion of the vertical Coriolis force in the equation is straightforward and irrelevant to the double predictor–corrector procedure that will be presented in the next section. For simplicity, the Coriolis acceleration in the vertical direction and the Coriolis effects due to the vertical velocity are not included in the above equations of motion.

The model also solves the following transport equation of concentration (e.g. salinity, temperature, suspended sediment concentration, etc.):

$$\frac{\partial c}{\partial t}+\frac{\partial uc}{\partial x}+\frac{\partial vc}{\partial y}+\frac{\partial wc}{\partial z}=\frac{\partial}{\partial x}\left(B_{\mathrm{h}}\frac{\partial c}{\partial x}\right)+\frac{\partial}{\partial y}\left(B_{\mathrm{h}}\frac{\partial c}{\partial y}\right)+\frac{\partial}{\partial z}\left(B_{\mathrm{v}}\frac{\partial c}{\partial z}\right)+S_{\mathrm{s}} \tag{5}$$

where c is concentration, S_{s} represents source/sink terms, and B_{h} and B_{v} represent horizontal and vertical eddy viscosities, respectively.

In Equations (2)–(5), the horizontal eddy viscosity and diffusivity (A_{h} and B_{h}) are computed from a sub-grid scale model [9], while the vertical eddy viscosity and diffusivity (A_{v} and B_{v}) are calculated by solving the turbulent kinetic energy equation from the velocity gradient [10]. If the concentration simulated involves settling, w in Equation (5) includes the settling velocity of the substance.

Integration equation (1) over the water column yields

$$\frac{\partial \eta}{\partial t}=-\frac{\partial}{\partial x}\left(\int_{h_0}^{\eta}u\,\mathrm{d}z\right)-\frac{\partial}{\partial y}\left(\int_{h_0}^{\eta}v\,\mathrm{d}z\right)+r \tag{6}$$

where η is the surface elevation; h_0 is the bottom elevation; and r is the net rain intensity (rainfall minus evaporation).

Boundary conditions in the horizontal directions are specified with either free-surface elevations or velocities for open boundaries. At solid boundary, both the velocity component and the pressure gradient in the normal direction are set to zero. Boundary conditions specified in the vertical direction are shear stresses. At the free surface, wind shear stresses are used. At the bottom, the loglayer distribution of velocity is used to calculate the bottom shear stresses, or

$$(\tau_x, \tau_y) = \rho \left[\frac{\kappa}{\ln(z_\mathrm{b}/z_o)} \right]^2 \sqrt{u_\mathrm{b}^2 + v_\mathrm{b}^2} (u_\mathrm{b}, v_\mathrm{b}) \tag{7}$$

where κ is the von Karman constant (0.41); u_b and v_b are horizontal velocities calculated at a level z_b near the bottom; $z_o = k_\mathrm{s}/30$ and k_s is the bottom roughness. Density in above equations is a function of temperature (T) and salinity (s) [11]:

$$\rho = \rho(T, s) \tag{8}$$

Pressure in Equations (2)–(4) includes both the hydrostatic (p_h) and non-hydrostatic (p_n) components. The hydrostatic component is obtained from Equation (4) by neglecting all the terms on the left hand side and the turbulent mixing terms on the right hand side:

$$p_\mathrm{h} = g \int_z^\eta \rho \, \mathrm{d}\xi \tag{9}$$

Therefore

$$p = p_\mathrm{n} + g \int_z^\eta \rho \, \mathrm{d}\xi \tag{10}$$

Using the Leibnitz integration law and the Boussinesq approximation, Equations (2)–(4) become

$$\frac{\partial u}{\partial t} = fv - g \frac{\partial \eta}{\partial x} - \frac{g}{\rho_o} \int_z^\eta \frac{\partial \rho}{\partial x} \, \mathrm{d}\xi - \frac{1}{\rho_o} \frac{\partial p_\mathrm{n}}{\partial x} + H(u) + \frac{\partial}{\partial z} \left(A_\mathrm{v} \frac{\partial u}{\partial z} \right) \tag{11}$$

$$\frac{\partial v}{\partial t} = -fu - g \frac{\partial \eta}{\partial y} - \frac{g}{\rho_o} \int_z^\eta \frac{\partial \rho}{\partial y} \, \mathrm{d}\xi - \frac{1}{\rho_o} \frac{\partial p_\mathrm{n}}{\partial y} + H(v) + \frac{\partial}{\partial z} \left(A_\mathrm{v} \frac{\partial v}{\partial z} \right) \tag{12}$$

$$\frac{\partial w}{\partial t} = -\frac{1}{\rho_o} \frac{\partial p_\mathrm{n}}{\partial z} + H(w) + \frac{\partial}{\partial z} \left(A_\mathrm{v} \frac{\partial w}{\partial z} \right) \tag{13}$$

where ρ_o is the reference density and H is an operator including the convective terms and the horizontal eddy diffusivity terms. In the above equations, terms containing the horizontal free-surface gradients are the barotropic terms, while those containing the horizontal density gradients are baroclinic terms.

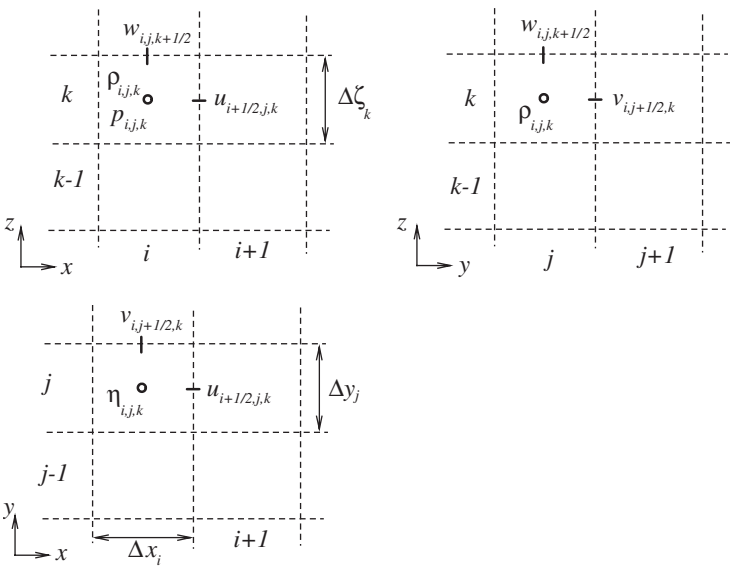

Figure 1. A Cartesian grid system used in the model with a staggered arrangement of model variables. The top-left graph is a view looking north, while the top-right and bottom graphs are views looking west and downward, respectively.

3. A DOUBLE PREDICTOR–CORRECTOR PROCEDURE

The numerical approach for solving the above equations is a finite difference scheme that involves two predictor–corrector steps. The model was developed in a Cartesian grid system with N_1, N_2, and N_3 grid cells in the west-east, south-north, and vertical directions, respectively. A staggered arrangement of model variables was used in the model. Figure 1 shows the horizontal and vertical views of the computational stencil in Cartesian co-ordinates. In Figure 1, Δx, Δy, and $\Delta\zeta$ are grid sizes in x-, y-, and z-directions, respectively and i, j, and k are grid indexes in the three directions. While Δx varies only with i, Δy varies only with j. $\Delta\zeta$ denotes the thickness of the horizontal layer, which is constant for the same k-index. To fit the bottom topography and the free surface, Δz for the actual cell height is used in the computation. Except for the bottom and top layers, Δz is the same as $\Delta\zeta$, the layer thickness. For the bottom layer, Δz is the distance between the top of the bottom layer and the real bottom. Similarly, for the top layer, Δz is the distance between the free surface and the bottom of the top layer. As a result, Δz is generally not the same as $\Delta\zeta$ for both the bottom and top layers. Because the centres of two neighbouring bottom cells are not necessarily at the same z-level, some numerical diffusion can be introduced in calculating horizontal gradients. To reduce the numerical diffusion, values at the centre of the bottom cell are interpolated to the centre of the layer before horizontal gradients are calculated. To ensure the vertical resolution near the free surface, the k-index for the top layer is allowed to vary with horizontal location and time. This eliminates the use of a thick top layer to cover the free-surface variation and allows the surface to travel from one layer to another. At each time step, the k-index for the top layer (k_m) is calculated and saved. If the free surface at the

$(n+1)$th time step drops below the middle point of the top layer, the top cell is aggregated to the cell below it and k_m is reduced by 1. On the other hand, if the free surface at the new time step is higher than the middle point of Layer k_m+1, the top cell at the previous time step is split into two cells and the top one is the new top cell at the new time step.

With a staggered arrangement of model variables, u and v are computed at the centres of the east and north faces of the cell, respectively, while w is computed at the centre of the top face. Density (ρ), pressure (p), and the concentration are computed at the centre of the cell. The surface elevation (η) and water depth (D) are defined at the centre of the horizontal grid.

The model uses the following finite difference scheme to solve Equations (11)–(13):

$$\frac{u^{n+1}_{i+1/2,j,k}-u^{n}_{i+1/2,j,k}}{\Delta t}=-g\left[(1-\theta)\frac{\partial \eta^{n}}{\partial x}+\theta\frac{\partial \eta^{n+1}}{\partial x}\right]-\frac{g}{\rho_o}\int_z^{\eta}\frac{\partial \rho^{n}}{\partial x}\,\mathrm{d}\xi-\frac{1}{\rho_o}\frac{\partial p^{n+1}_{\mathrm{n}}}{\partial x}$$
$$+fv^{n+}_{i+1/2,j,k}+\mathbf{H}(u^{n})+\frac{\partial}{\partial z}\left(A_{\mathrm{v}}\frac{\partial u^{n+1}}{\partial z}\right) \tag{14}$$

$$\frac{v^{n+1}_{i,j+1/2,k}-v^{n}_{i,j+1/2,k}}{\Delta t}=-g\left[(1-\theta)\frac{\partial \eta^{n}}{\partial y}+\theta\frac{\partial \eta^{n+1}}{\partial y}\right]-\frac{g}{\rho_o}\int_z^{\eta}\frac{\partial \rho^{n}}{\partial y}\,\mathrm{d}\xi-\frac{1}{\rho_o}\frac{\partial p^{n+1}_{\mathrm{n}}}{\partial y}$$
$$-fu^{n+}_{i,j+1/2,k}+\mathbf{H}(v^{n})+\frac{\partial}{\partial z}\left(A_{\mathrm{v}}\frac{\partial v^{n+1}}{\partial z}\right) \tag{15}$$

$$\frac{w^{n+1}_{i,j,k+1/2}-w^{n}_{i,j,k+1/2}}{\Delta t}=-\frac{\partial p^{n+1}_{\mathrm{n}}}{\partial z}+\mathbf{H}(w^{n})+\frac{\partial}{\partial z}\left(A_{\mathrm{v}}\frac{\partial w^{n+1}}{\partial z}\right) \tag{16}$$

where Δt is the time step, n represents the nth time step; θ is a parameter representing the implicitness (θ varies between 0 and 1); $\mathbf{H}$ is a finite difference operator for the convective terms and the horizontal eddy diffusivity terms.

In Equations (14)–(16), the non-hydrostatic pressure gradients and vertical eddy viscosity terms are discretized implicitly, while the water surface elevation gradients are discretized semi-implicitly with the implicitness θ. The semi-implicit treatment of the barotropic terms is necessary in order to avoid the time step being limited by the celerity of gravity waves and to reduce numerical dissipation. A fully explicit discretization of the barotropic terms ($\theta=0$) is undesirable even when the newly calculated velocity field is used to calculate the free-surface elevation (i.e. use u^n and v^n to calculate η^n and use u^{n+1} and v^{n+1} to calculate η^{n+1}), because the scheme will be constrained by the Courant number, defined as $C_r=\Delta t\sqrt{gD}/\Delta x$ where D is the water depth. With the free-surface elevation being calculated using the newly available velocity field, the scheme is stable only when C_r is not larger than 1 if the barotropic terms are treated fully explicitly. On the other hand, a fully implicit discretization ($\theta=1$) of the barotropic terms is quite dissipative [12], even though it has the advantage of being independent of the celerity of the gravity waves, or the Courant number can be larger than 1. The general guideline for choosing the implicitness parameter (θ) is: the scheme is unconditional stable with respect to gravity waves if $\theta\geqslant 0.5$, and the numerical dissipation reduces as θ is reduced from 1 to 0.5 [12].

Horizontal viscous terms in Equations (14)–(16) are treated explicitly. The Coriolis term is marked with the superscript '$n+$', which means that the newest available velocity component is always used in the computation. For example, when new u is first calculated from Equation (14), old v is used; however, when v is calculated from Equation (15), newly calculated u is used. To avoid that the calculation of v always uses a newer u-velocity, u and v are calculated in an alternate sequence: First calculate u then v at the odd time step, but reverse the sequence at the even time step.

It is rather cumbersome to directly solve Equations (14)–(16). In this paper, it is proposed to use two predictor–corrector steps to solve Equations (14)–(16). In the first predictor–corrector step, the hydrostatic pressure field at the previous time step is assumed to be the initial estimate of the total pressure field. In other words, the following equation is first solved:

$$\frac{u^{n++}_{i+1/2,j,k} - u^{n}_{i+1/2,j,k}}{\Delta t} = -g\frac{\partial \eta^n}{\partial x} - \frac{g}{\rho_o}\int_z^{\eta} \frac{\partial \rho^n}{\partial x}\,\mathrm{d}\xi + f v^{n+}_{i+1/2,j,k} + \mathbf{H}(u^n) + \frac{\partial}{\partial z}\left(A_{\mathrm{v}}\frac{\partial u^{n++}}{\partial z}\right) \tag{17}$$

$$\frac{v^{n++}_{i,j+1/2,k} - v^{n}_{i,j+1/2,k}}{\Delta t} = -g\frac{\partial \eta^n}{\partial y} - \frac{g}{\rho_o}\int_z^{\eta} \frac{\partial \rho^n}{\partial y}\,\mathrm{d}\xi - f u^{n+}_{i,j+1/2,k} + \mathbf{H}(v^n) + \frac{\partial}{\partial z}\left(A_{\mathrm{v}}\frac{\partial v^{n++}}{\partial z}\right) \tag{18}$$

$$\frac{w^{n++}_{i,j,k+1/2} - w^{n}_{i,j,k+1/2}}{\Delta t} = \mathbf{H}(w^n) + \frac{\partial}{\partial z}\left(A_{\mathrm{v}}\frac{\partial w^{n++}}{\partial z}\right) \tag{19}$$

where the subscript $n++$ denotes that the velocity field is an intermediate one because the pressure field is an estimated one.

In solving the above equations, the wind shear stresses specified at the free surface and the bottom shear stresses specified at the bed are Neumann-type boundary conditions. While the wind shear stresses are discretized at the half time step, the bottom shear stresses are discretized implicitly:

$$\left[A_{\mathrm{v}}\left(\frac{\partial u^{n++}}{\partial z}, \frac{\partial v^{n++}}{\partial z}\right)\right]_{z=\eta} = \frac{1}{\rho_\eta}(\tau_{\mathrm{w}x}^{n+1/2}, \tau_{\mathrm{w}y}^{n+1/2}) \tag{20}$$

$$\left[A_{\mathrm{v}}\left(\frac{\partial u^{n++}}{\partial z}, \frac{\partial v^{n++}}{\partial z}\right)\right]_{z=h_0} = \left[\frac{\kappa}{\ln(z_{\mathrm{b}}/z_o)}\right]^2 \sqrt{(u_{\mathrm{b}}^n)^2 + (v_{\mathrm{b}}^n)^2}(u_{\mathrm{b}}^{n++}, v_{\mathrm{b}}^{n++}) \tag{21}$$

where $\tau_{\mathrm{w}x}$ and $\tau_{\mathrm{w}y}$ denote wind shear stresses in the x- and y-directions, respectively; and ρ_η is the density at the free surface.

The velocity field solved (predicted) from Equations (17)–(19) does not necessarily satisfy the continuity equation for incompressible flows, because the hydrostatic pressure field at the nth time step is used in the equation. It is assumed that the velocity field will be divergence-free if the non-hydrostatic pressure gradients are added to Equations (17)–(19).

In other words, the velocity field calculated from the following equation will be divergence-free:

$$\frac{u_{i+1/2,j,k}^{n+^*} - u_{i+1/2,j,k}^{n}}{\Delta t} = -g\frac{\partial \eta^n}{\partial x} - \frac{g}{\rho_o}\int_z^{\eta}\frac{\partial \rho^n}{\partial x}\,\mathrm{d}\xi - \frac{1}{\rho_o}\frac{\partial p_{\mathrm{n}}^{n+1}}{\partial x} + f v_{i+1/2,j,k}^{n+} + \mathbf{H}(u^n) + \frac{\partial}{\partial z}\left(A_{\mathrm{v}}\frac{\partial u^{n+^*}}{\partial z}\right) \tag{22}$$

$$\frac{v_{i,j+1/2,k}^{n+^*} - v_{i,j+1/2,k}^{n}}{\Delta t} = -g\frac{\partial \eta^n}{\partial y} - \frac{g}{\rho_o}\int_z^{\eta}\frac{\partial \rho^n}{\partial y}\,\mathrm{d}\xi - \frac{1}{\rho_o}\frac{\partial p_{\mathrm{n}}^{n+1}}{\partial y} - f u_{i,j+1/2,k}^{n+} + \mathbf{H}(v^n) + \frac{\partial}{\partial z}\left(A_{\mathrm{v}}\frac{\partial v^{n+^*}}{\partial z}\right) \tag{23}$$

$$\frac{w_{i,j,k+1/2}^{n+^*} - w_{i,j,k+1/2}^{n}}{\Delta t} = -\frac{1}{\rho_o}\frac{\partial p_{\mathrm{n}}^{n+1}}{\partial z} + \mathbf{H}(w^n) + \frac{\partial}{\partial z}\left(A_{\mathrm{v}}\frac{\partial w^{n+^*}}{\partial z}\right) \tag{24}$$

Subtracting Equations (17)–(19), respectively, from Equations (22)–(24), the following equations for the velocity corrections ($u^{n+^*} - u^{n++}$, $v^{n+^*} - v^{n++}$, and $w^{n+^*} - w^{n++}$) are obtained:

$$\frac{u_{i+1/2,j,k}^{n+^*} - u_{i+1/2,j,k}^{n++}}{\Delta t} = -\frac{1}{\rho_o}\frac{\partial p_{\mathrm{n}}^{n+1}}{\partial x} + \frac{\partial}{\partial z}\left[A\frac{\partial (u^{n+^*} - u^{n++})}{\partial z}\right] \tag{25}$$

$$\frac{v_{i,j+1/2,k}^{n+^*} - v_{i,j+1/2,k}^{n++}}{\Delta t} = -\frac{1}{\rho_o}\frac{\partial p_{\mathrm{n}}^{n+1}}{\partial y} + \frac{\partial}{\partial z}\left[A\frac{\partial (v^{n+^*} - v^{n++})}{\partial z}\right] \tag{26}$$

$$\frac{w_{i,j,k+1/2}^{n+^*} - w_{i,j,k+1/2}^{n++}}{\Delta t} = -\frac{1}{\rho_o}\frac{\partial p_{\mathrm{n}}^{n+1}}{\partial z} + \frac{\partial}{\partial z}\left[A\frac{\partial (w^{n+^*} - w^{n++})}{\partial z}\right] \tag{27}$$

Taking x-, y-, and z-derivatives on both sides of the above three equations, respectively and adding them together, one obtains a Poisson equation for the non-hydrostatic pressure at the new time step as follows:

$$\nabla^2 p_{\mathrm{n}}^{n+1} = \frac{\rho_o}{\Delta t}\tilde{u} - \rho\frac{\partial}{\partial z}\left(A\frac{\partial \tilde{u}}{\partial z}\right) \tag{28}$$

where $\tilde{u} = \nabla\cdot(u_1^{n++}\mathbf{i} + u_2^{n++}\mathbf{j} + u_3^{n++}\mathbf{k})$, or the divergence of the first intermediate velocity field.

The model solves the above elliptic equation with the following boundary conditions for p_{n}^{n+1}: at the solid boundary (lateral and bottom), the normal gradient of p_{n}^{n+1} is zero; at the open boundary, p_{n}^{n+1} is either given or assumed to have a zero gradient; at the free surface, p_{n}^{n+1} is assumed to be zero.

Starting from the southwest corner of the computation domain and doing a three-dimensional loop, Equation (28) can be written for each grid cell, forming a seven-diagonal matrix system with a known right hand side after the first intermediate velocity field is solved. The

seven diagonals are saved in seven one-dimensional arrays using an index $l=(k-1)N_xN_y+(j-1)N_x+i$, where N_x and N_y are total numbers of grids in x- and y-directions, respectively. The seven-diagonal matrix system will take the following form:

$$\begin{aligned} &R^{3-}_{i,j,k}\,p^{n+1}{}_{\mathrm{n}\,i,j,k-1}+R^{2-}_{i,j,k}\,p^{n+1}{}_{\mathrm{n}\,i,j-1,k}+R^{1-}_{i,j,k}\,p^{n+1}{}_{\mathrm{n}\,i-1,j,k}\\ &\quad-(R^{3-}_{i,j,k}+R^{2-}_{i,j,k}+R^{1-}_{i,j,k}+R^{1+}_{i,j,k}+R^{2+}_{i,j,k}+R^{3+}_{i,j,k})\,p^{n+1}{}_{\mathrm{n}\,i,j,k}\\ &\quad+R^{1+}_{i,j,k}\,p^{n+1}{}_{\mathrm{n}\,i+1,j,k}+R^{2+}_{i,j,k}\,p^{n+1}{}_{\mathrm{n}\,i,j+1,k}+R^{3+}_{i,j,k}\,p^{n+1}{}_{\mathrm{n}\,i,j,k+1}=\frac{\rho_o}{\Delta t}\,\tilde{u}-\rho\,\frac{\partial}{\partial z}\left(A\,\frac{\partial\tilde{u}}{\partial z}\right) \end{aligned} \tag{29}$$

where

$$(R^{1\pm}_{i,j,k},R^{2\pm}_{i,j,k},R^{3\pm}_{i,j,k})=\left(\frac{1}{\Delta x_i\Delta x_{i\pm1/2}},\frac{1}{\Delta y_j\Delta y_{j\pm1/2}},\frac{1}{\Delta z_k\Delta z_{k\pm1/2}}\right) \tag{30}$$

If the grid sizes are uniformly distributed, the seven-diagonal matrix of Equation (29) is positive definite and can be solved using the conjugate gradient method with incomplete Cholesky preconditioning [13]. If the grid sizes are not uniformly distributed in the computation domain, the seven-diagonal matrix is generally asymmetric. In this case, the biconjugate gradient method can be used to solve the matrix. In this paper, a variant of the biconjugate gradient method called Bi-CGSTAB method [14] is used. The Bi-CGSTAB method can provide relatively uniform convergence for non-symmetric matrices.

Once the non-hydrostatic pressure component at the new time step is solved, the intermediate velocity field calculated from Equations (17)–(19) can be corrected by using Equations (25)–(27). The newly corrected velocity field (u^{n+*}) satisfies the continuity equation for incompressible flows. To get the final solutions to Equations (14)–(16), the second predictor–corrector step is carried out using a FSC method [15]. The free-surface location at the $(n+1)$th time step will also be found in the second predictor–corrector step.

Subtracting Equations (22)–(23) from Equations (14)–(15), respectively, the following second set of velocity-correction equations can be obtained:

$$\begin{aligned} u^{n+1}_{i+1/2,j,k}-u^{n+*}_{i+1/2,j,k}&=-\Delta tg\theta\,\frac{\partial(\eta^{n+1}-\eta^n)}{\partial x}+\Delta t\,\frac{\partial}{\partial z}\left[A\,\frac{\partial(u^{n+1}-u^{n+*})}{\partial z}\right]\\ v^{n+1}_{i,j+1/2,k}-v^{n+*}_{i,j+1/2,k}&=-\Delta tg\theta\,\frac{\partial(\eta^{n+1}-\eta^n)}{\partial y}+\Delta t\,\frac{\partial}{\partial z}\left[A\,\frac{\partial(v^{n+1}-v^{n+*})}{\partial z}\right] \end{aligned} \tag{31}$$

Integrating the above equation over the water column at the east and north faces of the grid yields

$$\begin{aligned} U^{n+1}_{i+1/2,j}-U^{n+*}_{i+1/2,j}&=-g\Delta t\theta\,\frac{\partial(\eta^{n+1}-\eta^n)}{\partial x}\,A^n_{i+1/2,j}\\ V^{n+1}_{i,j+1/2}-V^{n+*}_{i,j+1/2}&=-g\Delta t\theta\,\frac{\partial(\eta^{n+1}-\eta^n)}{\partial y}\,A^n_{i,j+1/2} \end{aligned} \tag{32}$$

where $A^n_{i+1,j}$ and $A^n_{i,j+1/2}$ are total areas of the east and north faces of the water column for a horizontal grid with the indexes i and j at the nth time step; and $U_{i+1/2,j}$ and $V_{i,j+1/2}$ are total mass fluxes through the east and north faces of the grid:

$$U_{i+1/2,j} = \sum_{k=k_{un}}^{k_{um}} u_{i+1/2,j,k} a^n_{i+1/2,j,k}, \qquad V_{i,j+1/2} = \sum_{k=k_{vn}}^{k_{vm}} v_{i,j+1/2,k} a^n_{i,j+1/2,k} \tag{33}$$

where $a^n_{i+1/2,j,k}$ and $a^n_{i,j+1/2,k}$ are areas of the east and north faces, respectively, of the cell with the indexes i, j, and k at the previous time step; k_{un} and k_{um} are, respectively, the bottom and top k-indexes at the east face of the grid; and k_{vn} and k_{vm} are the bottom and top k-indexes at the north face of the grid. Notice that the vertical eddy viscosity terms are not included in Equation (32). The reason for this is that the internal shear stresses are canceled out in the integration and the same wind shear stresses and bottom shear stresses are used to specify the Neumann-type boundary conditions for (u^{n+1}, v^{n+1}) and (u^{n+^*}, v^{n+^*}) at free surface and the bed, respectively.

The vertically integrated continuity equation, Equation (6), is discretized using the following semi-implicit scheme with the implicitness θ:

$$\Delta\eta_{i,j} = \eta^{n+1}_{i,j} - \eta^n_{i,j} = -\frac{\Delta t(1-\theta)}{a^\tau_{i,j}} [U^n_{i+1/2,j} - U^n_{i-1/2,j} + V^n_{i,j+1/2} - V^n_{i,j-1/2}]$$

$$- \frac{\Delta t\theta}{a^\tau_{i,j}} [U^{n+1}_{i+1/2,j} - U^{n+1}_{i-1/2,j} + V^{n+1}_{i,j+1/2} - V^{n+1}_{i,j-1/2}] + \Delta t\, r^{n+1/2}_{i,j} \tag{34}$$

where $\Delta\eta$ $(=\eta^{n+1} - \eta^n)$ is the final increment of the free surface over the time step Δt and $a^\tau_{i,j}$ is the wet surface area of the horizontal grid with the indexes i and j at the previous time step.

Combining Equations (32) and (34), one obtains

$$\eta^{n+1}_{i,j} - \eta^{n+^*}_{i,j} = \frac{g\Delta t^2\theta^2}{a^\tau_{i,j}} \left[A^n_{i+1/2,j} \frac{\Delta\eta_{i+1,j} - \Delta\eta_{i,j}}{\Delta x_{i+1/2}} - A^n_{i-1/2,j} \frac{\Delta\eta_{i,j} - \Delta\eta_{i-1,j}}{\Delta x_{i-1/2}} \right.$$

$$\left. + A^n_{i,j+1/2} \frac{\Delta\eta_{i,j+1} - \Delta\eta_{i,j}}{\Delta y_{j+1/2}} - A^n_{i,j-1/2} \frac{\Delta\eta_{i,j} - \Delta\eta_{i,j-1}}{\Delta y_{j-1/2}} \right] \tag{35}$$

where $\eta^{n+^*}_{i,j}$ is an intermediate free-surface elevation calculated from the velocity field at the previous time step and the intermediate velocity field (u^{n+^*}, v^{n+^*}) with the following semi-implicit discretization:

$$\eta^{n+^*}_{i,j} = \eta^n_{i,j} - \frac{\Delta t(1-\theta)}{a^\tau_{i,j}} [U^n_{i+1/2,j} - U^n_{i-1/2,j} + V^n_{i,j+1/2} - V^n_{i,j-1/2}]$$

$$- \frac{\Delta t\theta}{a^\tau_{i,j}} [U^{n+^*}_{i+1/2,j} - U^{n+^*}_{i-1/2,j} + V^{n+^*}_{i,j+1/2} - V^{n+^*}_{i,j-1/2}] + \Delta t\, r^{n+1/2}_{i,j} \tag{36}$$

Equation (35) can be seen as a free-surface correction equation [15], which adjusts the intermediate free-surface elevation by the amount of the right hand side of the equation. Equation (35) can be written as

$$\begin{aligned} &-R^s_{i,j}\Delta\eta_{i,j-1} - R^w_{i,j}\Delta\eta_{i-1,j} + (1 + R^s_{i,j} + R^w_{i,j} + R^e_{i,j} + R^n_{i,j})\Delta\eta_{i,j} - R^e_{i,j}\Delta\eta_{i+1,j} \\ &-R^n_{i,j}\Delta\eta_{i,j+1} = \eta^{n+*}_{i,j} - \eta^n_{i,j} \end{aligned} \tag{37}$$

where

$$\begin{aligned} R^w_{i,j} &= \frac{g\Delta t^2\theta^2}{a^\tau_{i,j}\Delta x_{i-1/2}} A_{i-1/2,j}, \qquad R^e_{i,j} = \frac{g\Delta t^2\theta^2}{a^\tau_{i,j}\Delta x_{i+1/2}} A_{i+1/2,j} \\ R^s_{i,j} &= \frac{g\Delta t^2\theta^2}{a^\tau_{i,j}\Delta y_{j-1/2}} A_{i,j-1/2}, \qquad R^n_{i,j} = \frac{g\Delta t^2\theta^2}{a^\tau_{i,j}\Delta y_{j+1/2}} A_{i,j+1/2} \end{aligned} \tag{38}$$

For an open boundary grid where the water level is known, the Dirichlet-type boundary condition is used: $\Delta\eta = \eta^{n+1} - \eta^n$. For a solid boundary or an open boundary where the flow rate is given, the Neumann-type boundary condition is used with a zero gradient of $\Delta\eta$ in the normal direction.

Equation (37) forms a five-diagonal matrix system similar to the seven-diagonal matrix system of Equation (29). For a uniformly distributed mesh, the five-diagonal matrix is positive definite and can be solved using the conjugate gradient method with incomplete Cholesky preconditioning [13]. If the grid sizes are not uniformly distributed in the computation domain, the Bi-CGSTAB method is used. The solution to Equation (37) gives the final free-surface location. The final velocity components in the x- and y-directions are calculated as follows [15]:

$$\begin{aligned} u^{n+1}_{i+1/2,j,k} &= u^{n+*}_{i+1/2,j,k} - \Delta tg\theta \frac{\partial(\eta^{n+1} - \eta^n)}{\partial x} \\ v^{n+1}_{i,j+1/2,k} &= v^{n+*}_{i,j+1/2,k} - \Delta tg\theta \frac{\partial(\eta^{n+1} - \eta^n)}{\partial y} \end{aligned} \tag{39}$$

It should be pointed out that Equations (39) and (31) are identical because $u^{n+1}_{i,j,k}$ and $v^{n+1}_{i,j,k}$ calculated from Equation (39) obviously satisfy Equation (31). This means that the second correction of the horizontal velocity components simply gives the second intermediate values some displacements determined by the second terms on the right hand side of Equation (39) [15].

The final vertical velocity is calculated as follows:

$$w^{n+1}_{i,j,k+1/2} = \frac{a_{i,j,k-1/2}}{a_{i,j,k+1/2}} w^{n+1}_{i,j,k-1/2} + \frac{U^{n+1}_{i-1/2,j,k} - U^{n+1}_{i+1/2,j,k} + V^{n+1}_{i,j-1/2,k} - V^{n+1}_{i,j+1/2,k}}{a_{i,j,k+1/2}} \tag{40}$$

where $a_{i,j,k+1/2}$ is the area of the top face of the cell with the indexes i, j, and k.

The above double predictor–corrector procedure for solving the final velocity field and the free-surface location at the $(n+1)$th time step can be summarized as follows:

1. Calculate the first intermediate velocity field $(u^{n++}, v^{n++}, w^{n++})$ using Equations (17)–(19), and save the results to 3-D arrays u, v, and w in the model,

2. Calculate the divergence of the newly calculated velocity field,
3. Solve the Poisson equation for non-hydrostatic pressure (p_{n}^{n+1}),
4. Calculate the second intermediate velocity field ($u^{n+*}, v^{n+*}, w^{n+*}$) using Equations (22)–(24), and save the results to the 3-D arrays u, v, and w (u^{n++}, v^{n++} and w^{n++} in the arrays are replaced by u^{n+*}, v^{n+*}, and w^{n+*}, respectively),
5. Calculate the intermediate free-surface elevation using Equation (36) with the velocity field at the previous time step and horizontal velocity components saved in arrays u and v,
6. Solve Equation (37) to obtain the change of the free-surface elevation over the time step Δt.
7. Calculate the final velocity field using Equations (39) and (40).

During the model run, if Steps (2)–(4) are omitted, then the simulation does not include non-hydrostatic pressure, or the model run is a hydrostatic simulation. Obviously, there is no need to compute w^{n++} in the first step for a hydrostatic simulation. Also, in calculating the intermediate free-surface elevation using Equation (36), u^{n++} and v^{n++} are treated as u^{n+*} and v^{n+*} if non-hydrostatic pressure is not included.

After the final velocity field and the free-surface location at the $(n+1)$th time step are found, the transport equation is solved. The numerical scheme used in the model for the transport equation is a flux-based finite difference scheme and takes the following form

$$\frac{c_{i,j,k}^{n+1} - c_{i,j,k}^{n}}{\Delta t} = S_S + \frac{1}{\forall_{i,j,k}^{n}} \left[\Delta F_x^n + \Delta F_y^n + \Delta F_z^n + \Delta f_x^n + \Delta f_y^n + a_{i,j,k+1/2}^n B_{\mathrm{v}i,j,k+1/2}^n \frac{c_{i,j,k+1}^{n+1} - c_{i,j,k}^{n+1}}{\Delta z_{k+1/2}^n} - a_{i,j,k-1/2}^n B_{\mathrm{v}i,j,k-1/2}^n \frac{c_{i,j,k}^{n+1} - c_{i,j,k-1}^{n+1}}{\Delta z_{k-1/2}^n} \right] \quad (41)$$

where $\forall_{i,j,k}^{n}$ is the water volume of the cell (varies with time for the top cell), ΔF_x^n, ΔF_y^n, and ΔF_z^n represent explicit discretizations of net advective fluxes of the material entering cell (i,j,k) in the x-, y-, and z-directions, respectively; and Δf_x^n and Δf_y^n are net diffusive fluxes of the concentration flowing into the cell from the x- and y-directions, respectively. Equation (33) is a tri-diagonal system and can be easily solved by the Thomas algorithm.

4. TESTS OF THE NUMERICAL SCHEME

The numerical method presented in the above section was tested with several analytical solutions and laboratory experiments. The first test is a two-dimensional, deepwater standing wave case in a rectangular basin with a depth of 10 m and a length of 10 m. The oscillation is caused by the following sinusoidal free-surface set-up at time = 0:

$$\eta = 10 + a\cos\left(\frac{\pi}{l}x\right) \quad (42)$$

where η is the free-surface elevation in meters (measured from the bottom of the basin); l is the length of the basin (10 m); and a is the wave amplitude (0.15 m).

The model used a uniform grid spacing of 0.2 m in the horizontal directions. In the vertical direction, the grid spacing varies between 0.1 and 0.3 m. From the dispersion relationship ($\sigma^2 = gk\tanh(kD)$, where $\sigma = 2\pi/T$, $k = 2\pi/L$, T is the wave period, $L = 2l_x$ is the wave length, and D is the average water depth), the wave period is calculated to be $T = 3.59$ s. Because this is a deepwater wave problem with small amplitude, the first order solution is accurate enough. Analytical solutions for this standing wave are [16]

$$\eta = 10 + a\cos kx\cos\sigma t \tag{43}$$

$$(u, w) = a\sigma\frac{\sin\sigma t}{\sinh kD}(\sin kx\cosh kz, -\cos kx\sinh kz) \tag{44}$$

where z is the vertical co-ordinate ($z = 0$ is at the bottom of the basin and $z = D$ is at the average water level); and u and w are velocities in the x- and z-directions, respectively.

The model was run for 10 s with a time step of 0.1 s. Time series of simulated surface elevations were printed out at $x = 0.1$ and 5.5 m. Also printed out were time series of velocities at two locations. The first location is at $x = 0.1$ m and $z = 8.9$ m, while the second one is at $x = 5.5$ m and $z = 4.9$ m. Figure 2 shows simulated time series of surface elevations and velocities at the two locations during the 10 s of the simulation period. The solid lines are simulated results, while the dashed lines represent the analytical solutions. Co-ordinates of the locations where comparison were made were also shown in the figure. As can be seen from Figure 2, simulated surface elevations at both locations agree well with analytical solutions. Simulated horizontal and vertical velocities are almost the same as analytical solutions. The wave period for the simulated oscillation is about 3.59 s, which is the same as that calculated from the dispersion relationship.

The model was also run using the hydrostatic pressure assumption for this seiche oscillation case. Figure 3 shows model results of the hydrostatic simulation. Again, solid lines are model results and dashed lines are analytical solutions. Because non-hydrostatic effect is significant, the hydrostatic pressure assumption is obviously not valid here. As expected, simulated oscillation using hydrostatic pressure is different from the analytical solution. As can be seen from Figure 3, without taking the non-hydrostatic effect into account, an initially linear wave becomes quite non-linear. High mode oscillation can be seen in simulated results, especially near the middle of the basin. The wave period of the simulated first mode oscillation is about 2 s, which is much shorter than the analytical solution of 3.59 s. The reason for a shorter oscillation period is that the hydrostatic pressure assumption forces the wave period to be $T = L(gD)^{1/2} = 2.02$ s.

Simulated velocity fields at $t = 8$ s for both the hydrostatic and fully hydrodynamic model runs are illustrated in Figure 4. The top panel of Figure 4 shows the velocity distribution with the consideration of the non-hydrostatic effects in the model run, while the bottom panel shows that without considering the non-hydrostatic effects. Again, the two panels in the figure are significantly different, not only in terms of velocity magnitude, but also in terms of the velocity direction. The fully hydrodynamic simulation predicts that water in the basin sloshes to the right end of the basin at $t = 8$ s. Nevertheless, the hydrostatic simulation predicts that it sloshes to the left end of the basin.

The second model validation is a finite amplitude seiche oscillation in a rectangular basin that is five meters deep and ten meters long. The seiching is a second mode oscillation caused

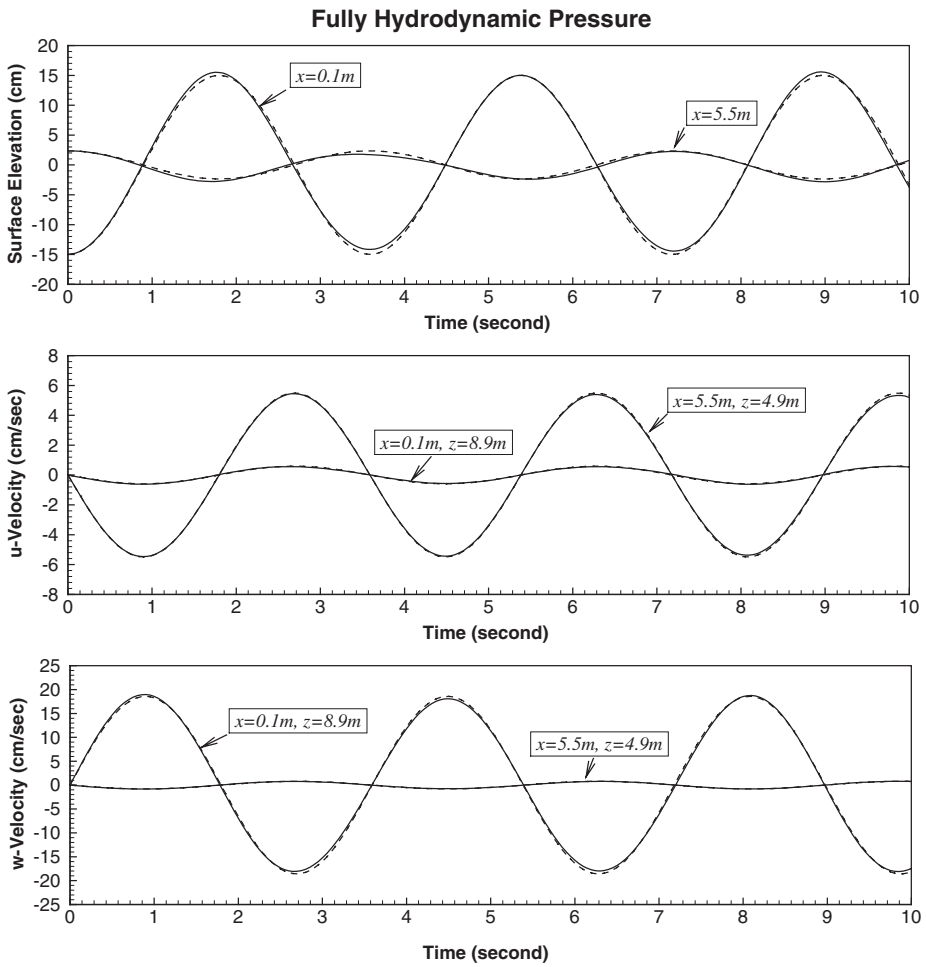

Figure 2. Simulated surface elevations and horizontal and vertical velocities (solid lines) including non-hydrostatic pressure. Model results are compared with analytical solutions (dashed lines). The top graph shows the surface elevation comparisons for $x = 0.1$ and 5.5 m, while the middle and bottom graphs show velocity comparisons at $x = 0.1$, $z = 8.9$ m and at $x = 5.5$, $z = 4.9$ m.

by a free-surface set-up at time $= 0$ with the following sinusoidal form:

$$\eta = 5 + a\cos\left(\frac{2\pi x}{l}\right) \tag{45}$$

where $a = 0.5$ m. The first order solution for this problem is

$$\eta(x,t) = 5 + a\cos(\omega_2 t)\cos(k_2 x) \tag{46}$$

where

$$k_m = \frac{m\pi}{l}, \quad \omega_m = \sqrt{k_m g \tanh(k_m D)} \tag{47}$$

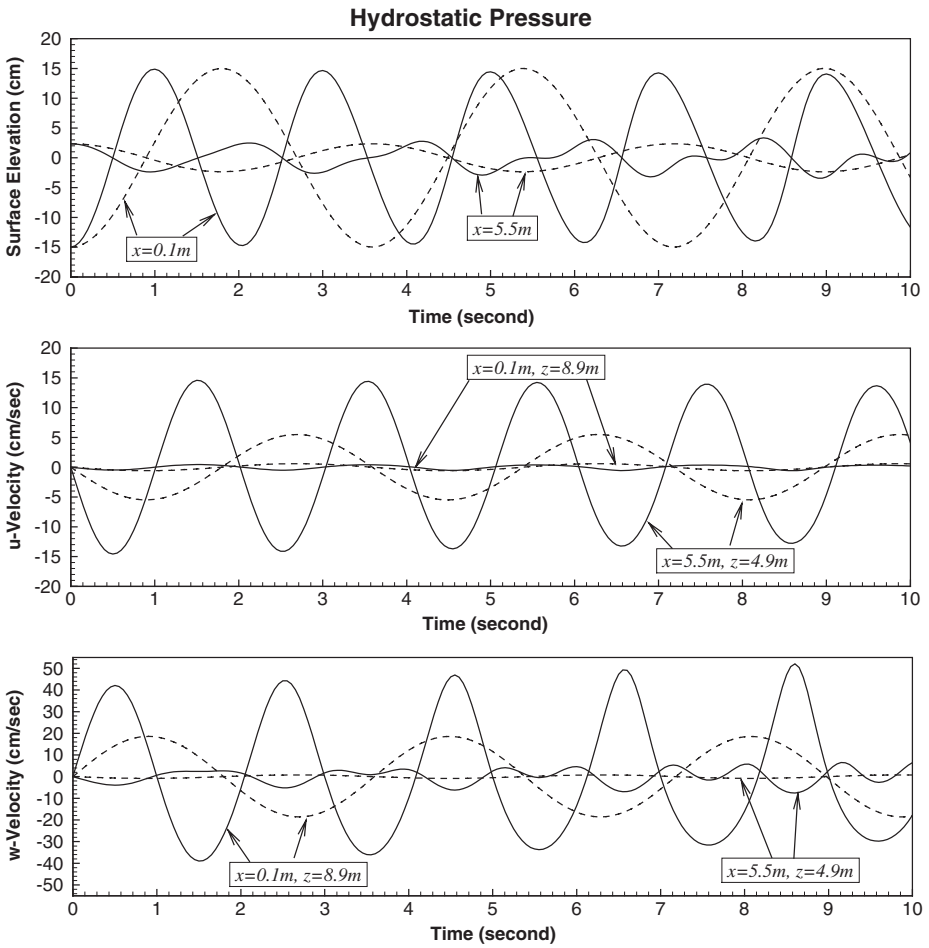

Figure 3. Simulated surface elevations and horizontal and vertical velocities (solid lines) using the hydrostatic assumption. Model results are compared with analytical solutions (dashed lines). The top graph shows the surface elevation comparisons for $x = 0.1$ and 5.5 m, while the middle and bottom graphs show velocity comparisons at $x = 0.1$, $z = 8.9$ m and at $x = 5.5$, $z = 4.9$ m.

Because the wave amplitude is about 10 per cent of the water depth, the first order wave alone is not sufficient. Wu and Eatlock Taylor [17] used the perturbation method to solve this problem and obtained the second order solution. At the centre of the basin, the second order surface elevation (the fourth mode oscillation) is

$$\eta_2\left(\frac{l}{2},t\right)=\frac{1}{8g}\left[2\omega_2^2a^2\cos(2\omega_2 t)+\frac{a^2}{\omega_2^2}(k_2^2g+\omega_2^4)-\frac{a^2}{\omega_2^2}(k_2^2g+3\omega_2^4)\cos(\omega_4 t)\right] \tag{48}$$

In the model simulation, a total of 50 grid cells were used in the x-direction with a uniform grid spacing of $\Delta x = 0.2$ m. In the vertical direction, 40 grid cells were used and the grid spacing varied between 0.1 and 0.2 m. The time step used was 0.05 s. The model was run with

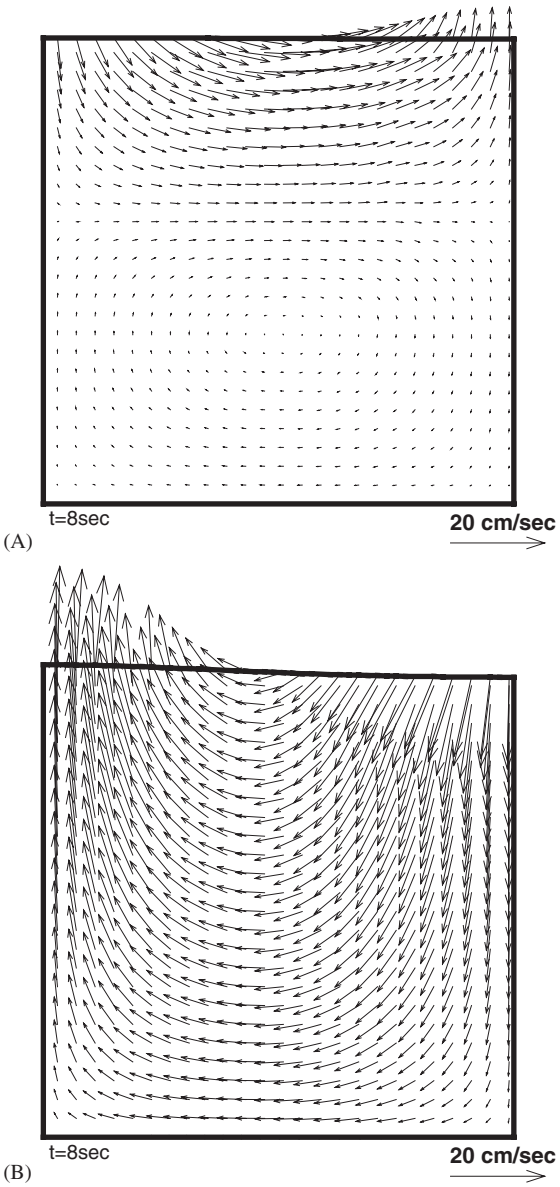

Figure 4. Simulated velocity fields at $t = 8$ s. The top panel (A) shows model results with the consideration of the non-hydrostatic effects, while the bottom panel (B) shows model results without the non-hydrostatic effects.

and without the consideration of the non-hydrostatic pressure component. Figure 4 shows the comparison of simulated surface elevation at the centre of the basin (solid line) with the first order elevation (dashed line) and the sum of the first and second order elevations (circles). It is clear that the model results are very close to the sum of the first and second order elevations.

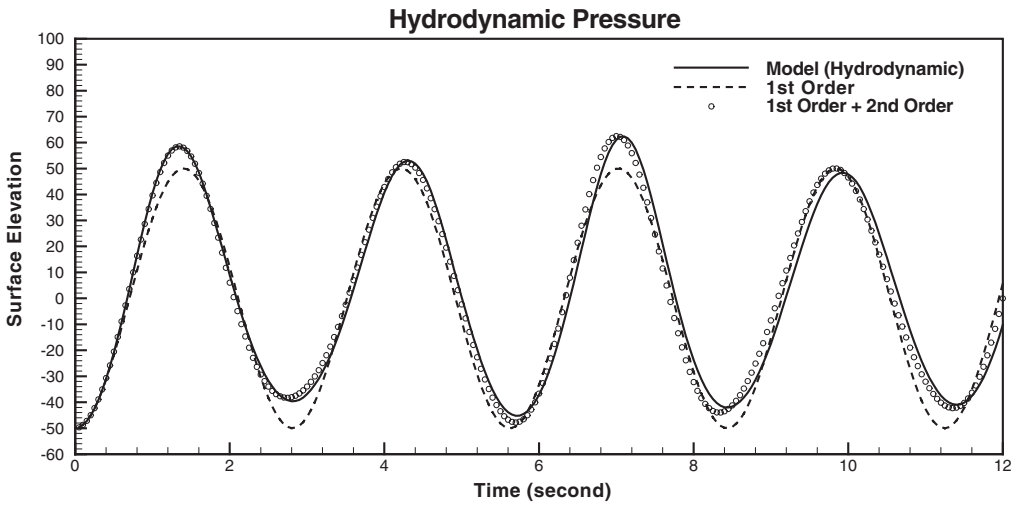

Figure 5. Simulated surface elevation at the centre of the basin versus the analytical solutions to the second order. Non-hydrostatic pressure was included in the simulation.

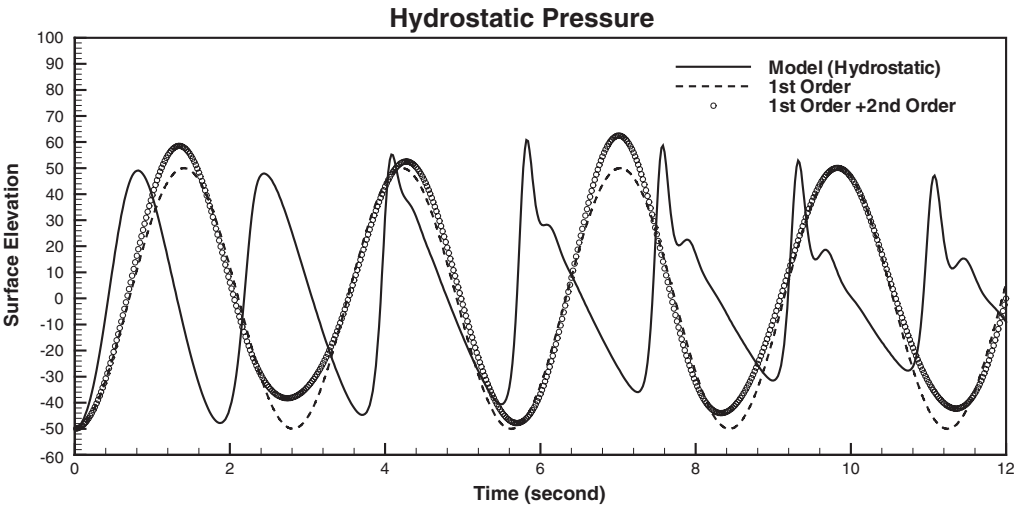

Figure 6. Simulated surface elevation at the centre of the basin versus the analytical solutions to the second order. Non-hydrostatic pressure was not included in the simulation.

In the model simulation shown in Figure 5, non-hydrostatic pressure was included. If the non-hydrostatic effect is excluded, model results will be totally different from the analytical solutions. Figure 6 shows simulated surface elevation at the centre of the basin without the non-hydrostatic effects. Similar to the hydrostatic simulation in the last test case, model results contain more non-linear components and the simulated first order wave has a wave period which is shorter than what is calculated from Equation (47) by about 35 per cent.

The next model test is a so-called lock-exchange problem. A rectangular basin with a length of $l_x = 0.4$ cm and a depth of 0.18 m has a gate at the half length of the basin that separates fresh water in the left half from salty water in the right half. At time < 0, the salinity distribution was

$$c = \begin{cases} 0, & x \leqslant l_x/2 \\ 4, & x > l_x/2 \end{cases} \tag{49}$$

where salinity (c) is in parts per thousand (ppt). At time $= 0$, the gate is removed and water starts to move under the baroclinic force caused by the horizontal density gradient.

A uniformly distributed grid system with $\Delta x = \Delta z = 0.01$ m was used for the model simulation of this lock-exchange problem. The time step used was 0.1 s. Again, two model runs were conducted: one used the hydrostatic pressure assumption and the other considered the non-hydrostatic effects. Figure 7 shows simulated velocity fields and salinity distributions with the consideration of the non-hydrostatic effects in the simulation, while Figure 8 shows model results without considering the non-hydrostatic effects. Both Figures 7 and 8 show model results at time $= 1.8$ and 3.8 s. Because of the localized horizontal density gradient in the vicinity of the freshwater/salt water interface, the non-hydrostatic effect on the flow is strong at and near the interface. Obviously, the model produced different velocity and salinity distributions with and without the non-hydrostatic effects. While the simulated salinity distribution with the hydrostatic assumption has a relatively sharp nose-shape front migrating from right to left, the simulated freshwater/salt water interface without the hydrostatic assumption is much smoother. The simulated salinity distributions shown in Figures 7 and 8 are similar to those in Casulli and Stelling [5] for a similar lock-exchange case. From Simpson [20] and Turner [21], the simulated interface without the hydrostatic assumption is more realistic, while the simulated interface with the hydrostatic assumption is unreal.

The simulated velocity of the hydrostatic simulation is generally larger than that of non-hydrostatic simulation, especially near the front where the water tends to move in the vertical direction. This in turn prevents the relatively sharp nose losing its shape while moving to the left side of the basin. Without considering the non-hydrostatic effects, simulated velocities mainly occur within a distinct box that expends from the middle of the basin to the two ends as time goes on. Outside the box, velocities are very small due to the lack of horizontal pressure gradient because both the baroclinic and barotropic forces are negligible for these areas. On the other hand, the simulated velocity field without the hydrostatic assumption does not show a distinct box and the streamlines are elliptical. Even for areas where the baroclinic effects have not yet reached, velocities are not minor. In fact, velocities in these area increases as time goes on due to the cumulative effects of non-hydrostatic pressure.

The last test of the numerical scheme is a laboratory experiment of a non-linear wave propagating over a bar towards a beach [18]. Cassulli and Stelling [5] tested their non-hydrodynamic model using the same laboratory experiment. The experiment was performed in a flume with a length of 30 m and a water depth of 0.4 m (Figure 9). A sinusoidal wave of 0.01 m with the period of 2.02 s propagates from the left end, over the bar, to the beach at the right end with a slop of 0.04.

In the model simulation, the simulation domain was discretized using a uniformly distributed grid system with the dimension of $\Delta x = \Delta z = 0.02$ m. The time step (Δt) used for the simulation was 0.04 s. The model can automatically handle the wetting/drying situation at the right

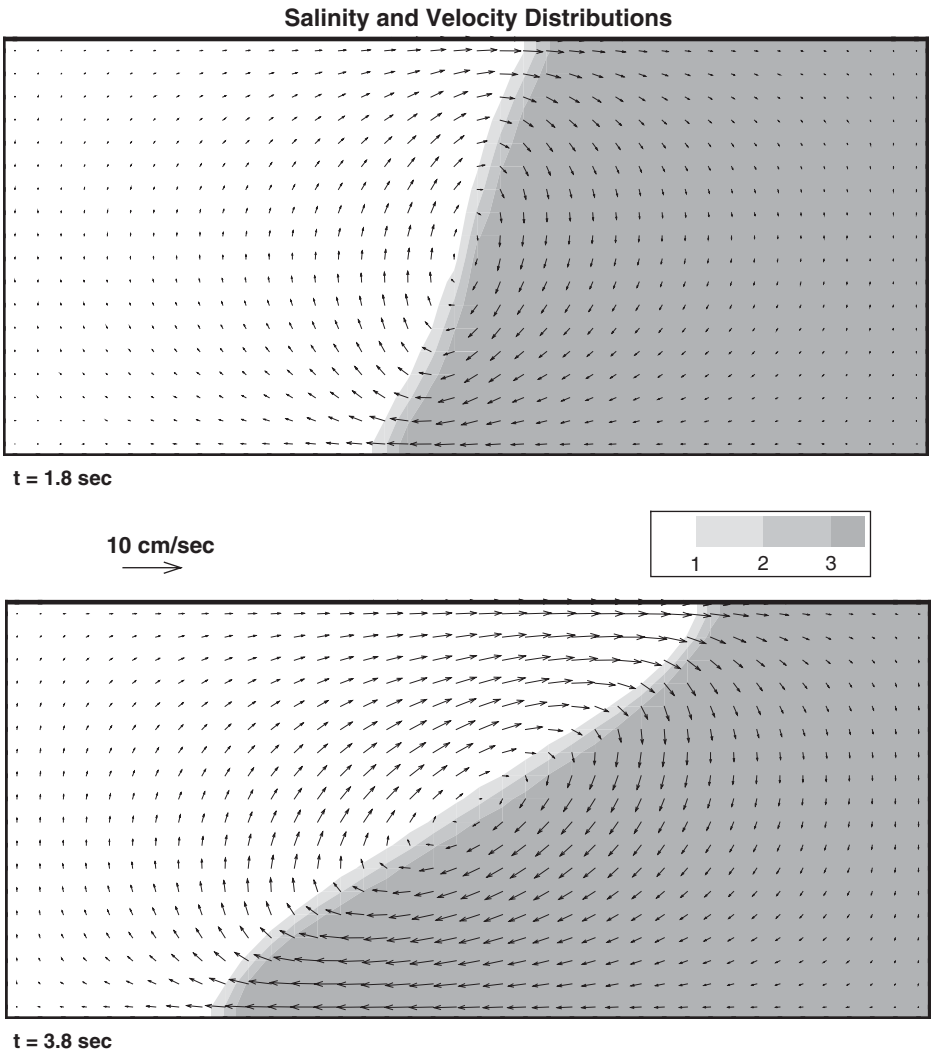

Figure 7. Simulated salinity and velocity distributions at $t = 1.8$ s (top graph) and 3.8 s (bottom graph) for the lock-exchange problem. The non-hydrostatic pressure component was included in the model run. The white area has a salinity of 0 ppt.

end of the flume using a method described in Reference [19]. The model was run both with and without non-hydrostatic pressure. Figure 10 shows comparisons of simulated free-surface elevations with measured data at A, B, C, and D with the consideration of non-hydrostatic pressure. Although model results can still be improved, the agreement between simulated and measured free-surface elevations at A, B, C, and D is much better than that without the non-hydrostatic effects. As shown in Figure 11, the hydrostatic simulation generates incorrect model results that are totally different from measured data. Obviously, a hydrostatic scheme won't be able to simulate this steep wave case, while the non-hydrodynamic scheme presented

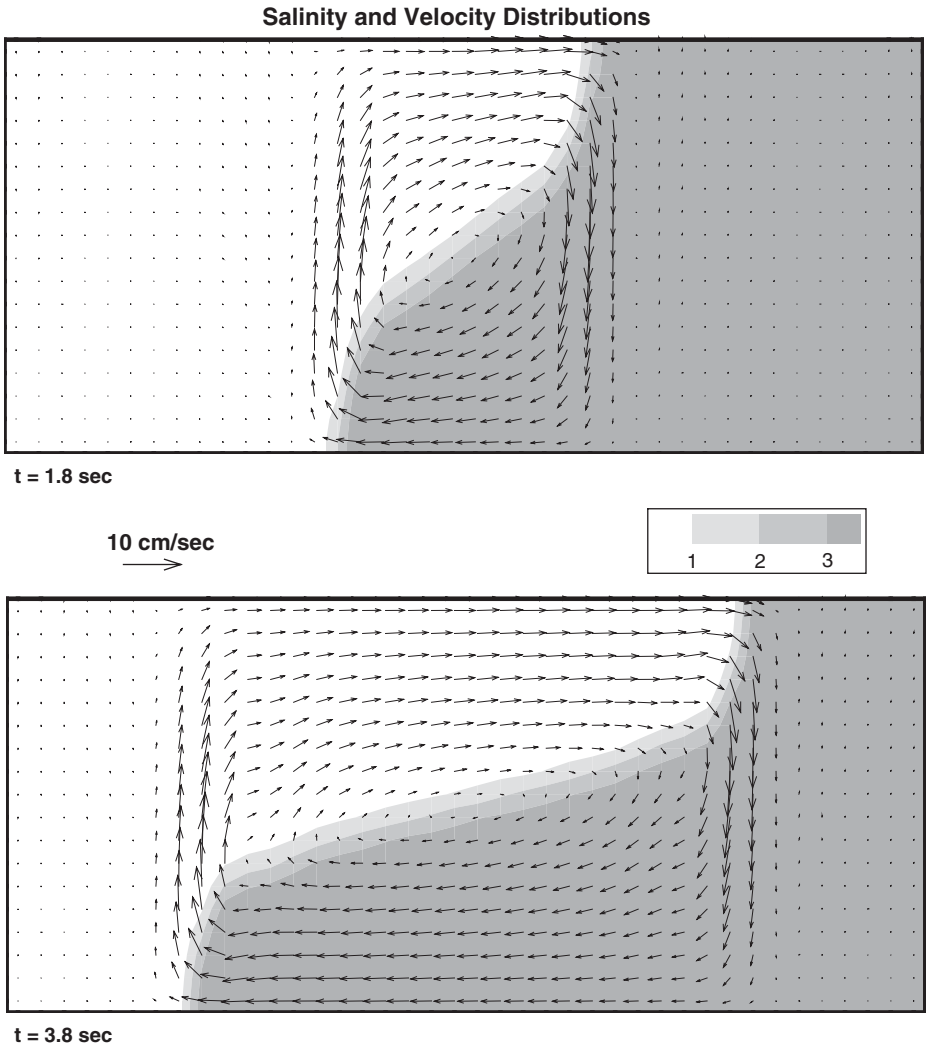

Figure 8. Simulated salinity and velocity distributions at $t = 1.8$ s (top graph) and 3.8 s (bottom graph) for the lock-exchange problem. The non-hydrostatic pressure component was not included in the model run. The white area has a salinity of 0 ppt.

in this paper has the ability to simulate such a complex wave propagating problem, which is normally simulated using Boussinesq equation models [18].

5. CONCLUSIONS

A three-dimensional, non-hydrostatic model has been developed. The model solves the RANS equations using a finite difference scheme that contains two predictor–corrector steps. In the

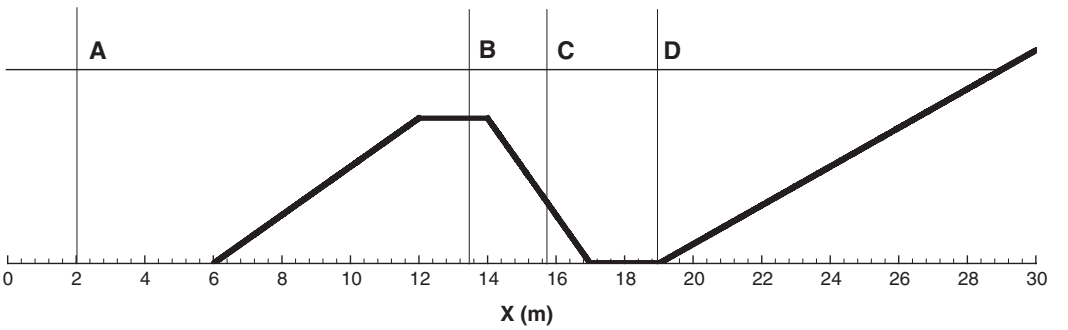

Figure 9. The geometry of the flume used to conduct a laboratory experiment of non-linear wave propagating over a bar toward a beach. The water depth decreases from 0.4 m at A to 0.1 m at B. The slope at the right end is 0.04. The water surface elevations measured include those at Stations A, B, C, and D located 2, 13.5, 15.7, and 19 m away from the open boundary, respectively.

first predictor–corrector step, the model uses the hydrostatic pressure at the previous time step as an initial estimate of the pressure field to calculate an intermediate velocity field. The estimated pressure field is corrected by adding the non-hydrostatic component. An elliptic equation for non-hydrostatic pressure is obtained by forcing the velocity field to satisfy the continuity equation for incompressible flows. After the non-hydrostatic pressure component is solved, a second intermediate velocity field is found, with which an intermediate free surface can be calculated. In the second predictor–corrector step, a FSC method is used to find the final free surface, before the second intermediate velocity field is further corrected to obtain the final solutions.

It can be clearly seen that the numerical scheme presented will be reduced to an explicit hydrostatic model if the two predictor–corrector steps are omitted. In this case, the first intermediate velocity field is treated as the final velocity field and is used to calculate the final free-surface elevation at the $(n+1)$th time step. If the first predictor–corrector step only is omitted, then the model is a semi-implicit hydrostatic model using the FSC method [15]. Therefore, the numerical scheme presented in this paper can be easily incorporated in existing hydrostatic models, even if they are explicit models. The solution procedure presented is different from some other non-hydrostatic models [4–6, 8] that calculate the free surface before non-hydrostatic pressure is solved. Instead, in the numerical procedure presented, the location of the free surface is found after non-hydrostatic pressure at the new time step is calculated. In other words, the calculated free-surface change over the time step (Δt) contains the non-hydrostatic effects in the numerical scheme presented.

The numerical scheme has been tested with several analytical solutions and laboratory experiments. In the four test cases presented, non-hydrostatic effects are important and cannot be neglected. As can be seen from the comparisons of model results with analytical solutions or laboratory data, the four test cases cannot be simulated without considering the non-hydrostatic effects. With the consideration of the non-hydrostatic effects, however, the numerical scheme presented is able to generate satisfactory model results. The comparisons to the two analytical solutions are good. For the lock-exchange case and the laboratory experiment of a non-linear wave propagating over a bar, although no analytical solutions are available, model results

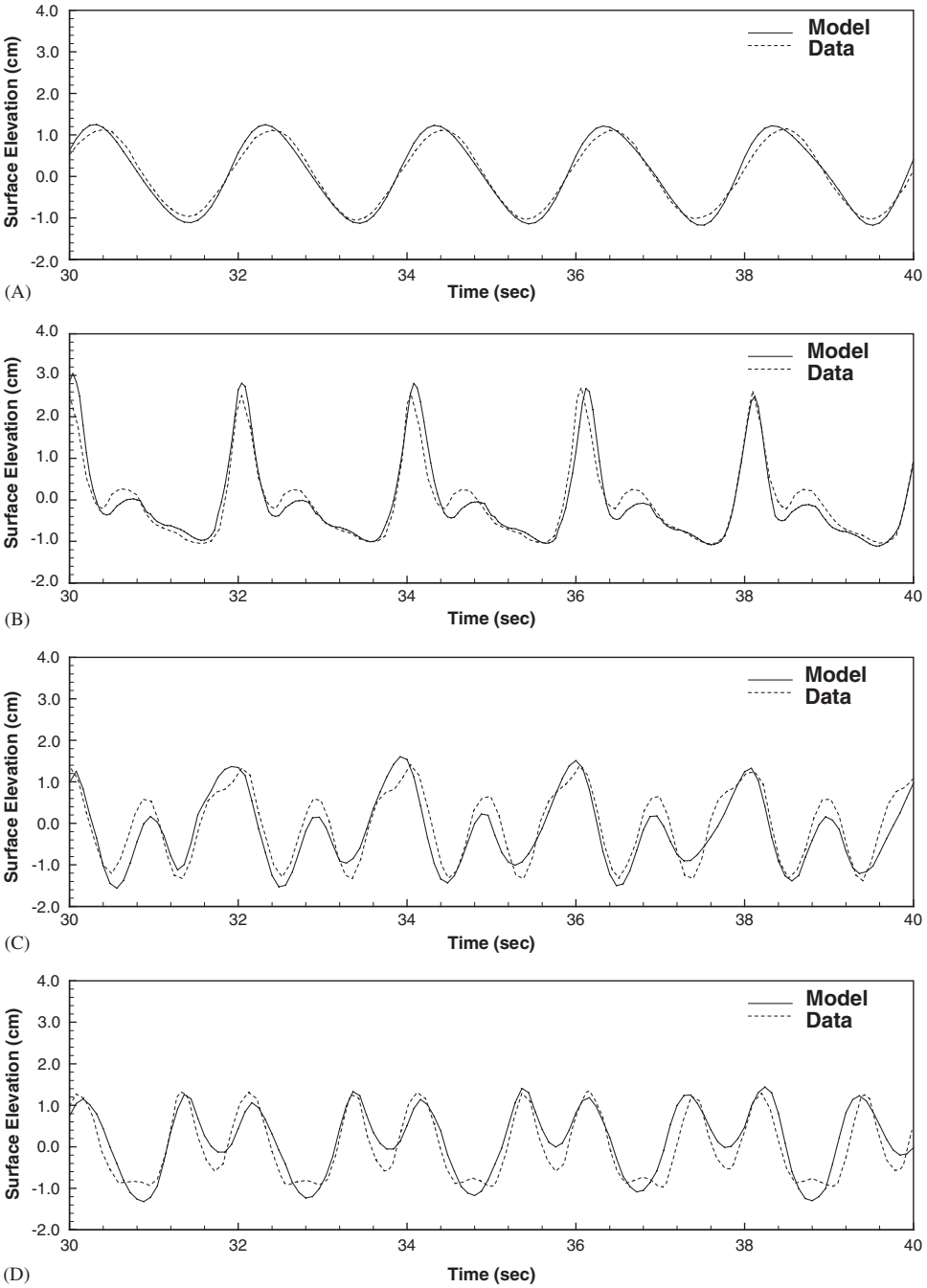

Figure 10. Comparison of simulated and measured surface elevations at A, B, C, and D with measured data. Non-hydrostatic pressure was included in the simulation.

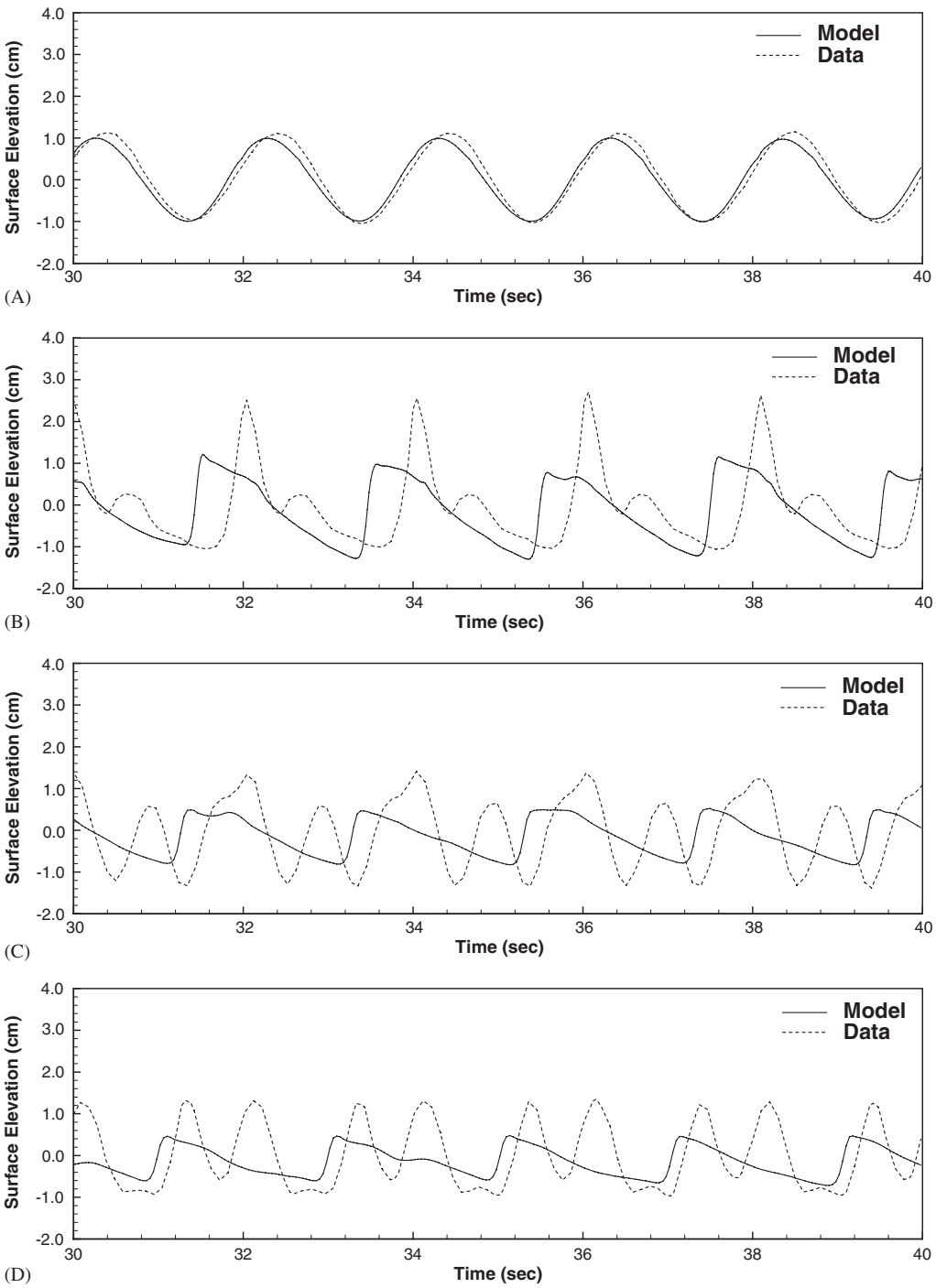

Figure 11. Comparison of simulated and measured surface elevations at A, B, C, and D with measured data. Non-hydrostatic pressure was not included in the simulation.

are similar to those in Casulli and Stelling [4] and agree fairly well with what was found in the laboratory. The four tests presented in the paper suggest that the proposed numerical method is suitable for simulating free-surface flows where the non-hydrostatic effects are important.

REFERENCES

1. Blumberg AF, Mellor GL. A description of a three-dimensional coastal ocean circulation model. *Three-Dimensional Coastal Ocean Models*, American Geophysical Union, 1987; 1–16.
2. Sheng YP. On modeling three-dimensional estuarine and marine hydrodynamics. In *Three-Dimensional Models of Marine and Estuarine Dynamics*, Nihoul JCJ, Jamart BM (eds). Elsevier Oceanography Series, Elsevier: Amsterdam, 1987; 35–54.
3. Hamrick JM. A three-dimensional environmental fluid dynamic computer code: theoretical and computational aspects. *Special Report in Applied Marine Science and Ocean Engineering*, No. 317. Virginia Institute of Marine Science, College of Willian & Mary, Gloucester Point, Virginia, 1992.
4. Casulli V, Stelling GS. Simulation of three-dimensional, non-hydrostatic free-surface flows for estuaries and coastal seas. In *Proceedings of the 4th International Conference on Estuarine and Coastal Modeling*, Spaulding ML, Cheng RT (eds), San Diego, California. ASCE: New York, 1995; 1–12.
5. Casulli V, Stelling GS. Numerical simulation of 3D quasi-hydrostatic free-surface flows. *Journal of Hydraulic Engineering* 1998; **124**(7):678–686.
6. Mahadevan A, Oliger J, Street R. A nonhydrostatic mesoscale ocean model. Part II: numerical implementation. *Journal of Physical Oceanography* 1996; **26**(9):1881–1900.
7. Jankowski JA. A non-hydrostatic model for free surface flows. *Ph.D. Dissertation*, University of Hannover, Germany, 1999.
8. Koçyigit MB, Falconer RA, Lin B. Three-dimensional numerical modeling of free surface flows with non-hydrostatic pressure. *International Journal for Numerical Methods in Fluids* 2002; **40**(9):1145–1162.
9. Smagorinsky J. General circulation experiments with primitive equations, I. The basic experiment. *Monthly Weather Review* 1963; **91**(3):99–164.
10. Chen X. Effects of hydrodynamics and sediment transport processes on nutrient dynamics in shallow lakes and estuaries. *Ph.D. Dissertation*, University of Florida, Gainesville, 1994.
11. UNESCO. Algorithms for computation of fundamental properties of seawater. *UNESCO Technical Papers in Marine Science*, Number 44, UNESCO, Paris, 1983; 53.
12. Casulli V, Cattani E. Stability, accuracy and efficiency of a semi-implicit method for three-dimensional shallow water flow. *Computers and Mathematics with Applications* 1994; **27**(4):99–112.
13. Golub GH, van Loan C. *Matrix Computations*. John Hopkins University Press: Baltimore, 1990.
14. Van der Vorst HA. Bi-CGSTAB: a fast and smoothly converging variant of Bi-CG for the solution of nonsymmetric linear systems. *SIAM Journal of Science Statistical Computing* 1992; **13**(2):631–644.
15. Chen X. A free-surface correction method for simulating shallow water flows. *Journal of Computational Physics* 2003; accepted for publication.
16. Lamb H. *Hydrodynamics*. Dover: New York, 1945.
17. Wu GX, Eatock Taylor R. Finite element analysis of two-dimensional non-linear transient water waves. *Applied Ocean Research* 1994; **16**:363–372.
18. Beji S, Battijes JA. Numerical simulation of nonlinear waves propagating over a bar. *Coastal Engineering* 1994; **23**(1/2):1–16.
19. Chen X. Fitting topography and shorelines in a 3-D, Cartesian-grid model for free-surface flows. *Proceedings of Second MIT Conference on Computational Fluid and Solid Mechanics*. Elsevier: Amsterdam, 2003; in press.
20. Simpson JE. *Gravity Currents in the Environment and in the Laboratory*. Ellis Horwood, Ltd.: Chichester, England, 1987.
21. Turner JS. *Buoyancy Effects in Fluids*. Cambridge University Press: New York, 1973.

